LETTER

doi:10.1038/nature25765

Sterically controlled mechanochemistry under hydrostatic pressure

Hao Yan[1,2]*, Fan Yang[1,3]*, Ding Pan[4,5,6]*, Yu Lin[1], J. Nathan Hohman[7], Diego Solis-Ibarra[8], Fei Hua Li[1,2], Jeremy E. P. Dahl[1], Robert M. K. Carlson[1], Boryslav A. Tkachenko[9], Andrey A. Fokin[9,10], Peter R. Schreiner[9], Giulia Galli[11], Wendy L. Mao[1,3], Zhi-Xun Shen[1,12] & Nicholas A. Melosh[1,2]

Mechanical stimuli can modify the energy landscape of chemical reactions and enable reaction pathways, offering a synthetic strategy that complements conventional chemistry[1–3]. These mechanochemical mechanisms have been studied extensively in one-dimensional polymers under tensile stress[4–9] using ring-opening[10] and reorganization[11], polymer unzipping[6,12] and disulfide reduction[13,14] as model reactions. In these systems, the pulling force stretches chemical bonds, initiating the reaction. Additionally, it has been shown that forces orthogonal to the chemical bonds can alter the rate of bond dissociation[15]. However, these bond activation mechanisms have not been possible under isotropic, compressive stress (that is, hydrostatic pressure). Here we show that mechanochemistry through isotropic compression is possible by molecularly engineering structures that can translate macroscopic isotropic stress into molecular-level anisotropic strain. We engineer molecules with mechanically heterogeneous components—a compressible ('soft') mechanophore and incompressible ('hard') ligands. In these 'molecular anvils', isotropic stress leads to relative motions of the rigid ligands, anisotropically deforming the compressible mechanophore and activating bonds. Conversely, rigid ligands in steric contact impede relative motion, blocking reactivity. We combine experiments and computations to demonstrate hydrostatic-pressure-driven redox reactions in metal–organic chalcogenides that incorporate molecular elements that have heterogeneous compressibility[16–19], in which bending of bond angles or shearing of adjacent chains activates the metal–chalcogen bonds, leading to the formation of the elemental metal. These results reveal an unexplored reaction mechanism and suggest possible strategies for high-specificity mechanosynthesis.

We demonstrate the molecular anvil concept (Extended Data Fig. 1) in copper(I) *m*-carborane-9-thiolate (Cu-S-M9) crystals (where *m* denotes the meta positions of the carbon atoms in the carborane), synthesized via ligand-directed assembly[16]. The unit cell (Fig. 1a, Extended Data Fig. 2 and Supplementary Table 1), determined by single-crystal X-ray diffraction (XRD), is composed of two enantiomers. Each molecule (Fig. 1b) has a Cu_4S_4 core surrounded by M9 ligands. These ligands are anticipated to be much more structurally rigid, owing to their cage-like nature, than the Cu_4S_4 core. Importantly, the distances between M9 groups (7.4–9.2 Å) are substantially larger than the molecular distance in *m*-carborane crystals (6.9 Å, ref. 17), indicating that the M9 groups are not in van der Waals contact, thus allowing them to move without mutual steric hindrance under compression.

We first show that hydrostatic pressure drives a Cu(I) to Cu(0) reduction in Cu-S-M9. Transmission electron microscopy (TEM) images of a sample after compression to 12 GPa reveals crystalline nanoclusters (Fig. 1c and d) with lattice spacing of 2.08 Å, consistent with the [111] spacing of face-centred cubic copper. Energy dispersive X-ray spectroscopy (EDS, Fig. 1e) shows that the nanoclusters are composed exclusively of copper and are free of sulfur, clearly different from the pristine Cu-S-M9 (Extended Data Fig. 3). These results indicate that Cu(I) in Cu-S-M9 is reduced to Cu(0) under hydrostatic pressure. Note that the average size of the Cu nanoclusters, about 10 nm, is not determined by the size of the starting crystal (1–100 μm, inset to Fig. 1c), but rather by the nucleation density and diffusivity of atomic copper at high pressure. Here the sulfur serves as the reducing agent, forming an oxidized species (for example, disulfide[20]), as revealed by X-ray photoelectron spectroscopy (Extended Data Fig. 4) and supported by density functional theory (DFT) computations discussed later.

This pressure-driven mechanochemical reaction takes a different pathway from conventional thermochemistry of the same compound. Heating Cu-S-M9 to 400 °C under vacuum yields cuprous sulfide (Extended Data Fig. 5) instead of elemental copper. Literature data also indicate that pyrolysis of a chemically similar compound, copper(I) *tert*-butylthiolate, yields cuprous sulfide[21].

The reactivity of the Cu-S-M9 system is pressure-dependent. We first note that elemental copper was observed only after compression beyond 8 GPa (Extended Data Fig. 3). To understand this threshold behaviour, we used *in situ* XRD to track the structural change of the system and its connection with reactivity. The XRD patterns below 8 GPa show well defined peaks corresponding to Cu-S-M9, which shift smoothly to increasing 2θ (decreasing the lattice spacing d) as pressure increases (vertical dotted lines, Fig. 1f). The unit cell volumes can be fitted to a third-order Birch–Murnaghan equation of state[22] (solid red line, Fig. 1g), consistent with elastic compression. Releasing the pressure after compression within this range fully restores the ambient diffraction pattern (Extended Data Fig. 6), suggesting no irreversible structural change. However, compression beyond 8 GPa results in missing diffraction peaks, and at 12 GPa all diffraction peaks related to Cu-S-M9 disappear (purple, Fig. 1f), indicating a disordered phase. The diffraction pattern of Cu-S-M9 is not restored after compression to this range (green, Fig. 1f), indicating irreversible structural change. The pressure range in which the crystalline-disorder transition occurs, 8–12 GPa, agrees well with the pressure window for elemental copper formation observed by TEM.

To establish that this change is due to a pressure-driven reaction, we examined the valence change of copper as a function of pressure. *In situ* X-ray absorption spectroscopy (XAS) shows that the intensity of

---

[1] Stanford Institute for Materials and Energy Sciences, SLAC National Accelerator Laboratory, Menlo Park, California 94025, USA. [2] Department of Materials Science and Engineering, Stanford University, Stanford, California 94305, USA. [3] Department of Geological Sciences, Stanford University, Stanford, California 94305, USA. [4] Department of Physics, Hong Kong University of Science and Technology, Hong Kong, China. [5] Department of Chemistry, Hong Kong University of Science and Technology, Hong Kong, China. [6] HKUST Fok Ying Tung Research Institute, Guangzhou, China. [7] The Molecular Foundry, Lawrence Berkeley National Laboratory, Berkeley, California 94720, USA. [8] Laboratorio de Fisicoquímica y Reactividad de Superficies (LaFReS), Instituto de Investigaciones en Materiales, Universidad Nacional Autónoma de México, Coyoacán, CDMX 04510, México. [9] Institute of Organic Chemistry, Justus-Liebig University, Heinrich-Buff-Ring 17, D-35392 Giessen, Germany. [10] Department of Organic Chemistry, Igor Sikorsky Kiev Polytechnic Institute, pr. Pobedy 37, 03056 Kiev, Ukraine. [11] Institute for Molecular Engineering, University of Chicago, Chicago, Illinois 60637, USA. [12] Department of Physics, Stanford University, Stanford, California 94305, USA.

*These authors contributed equally to this work.

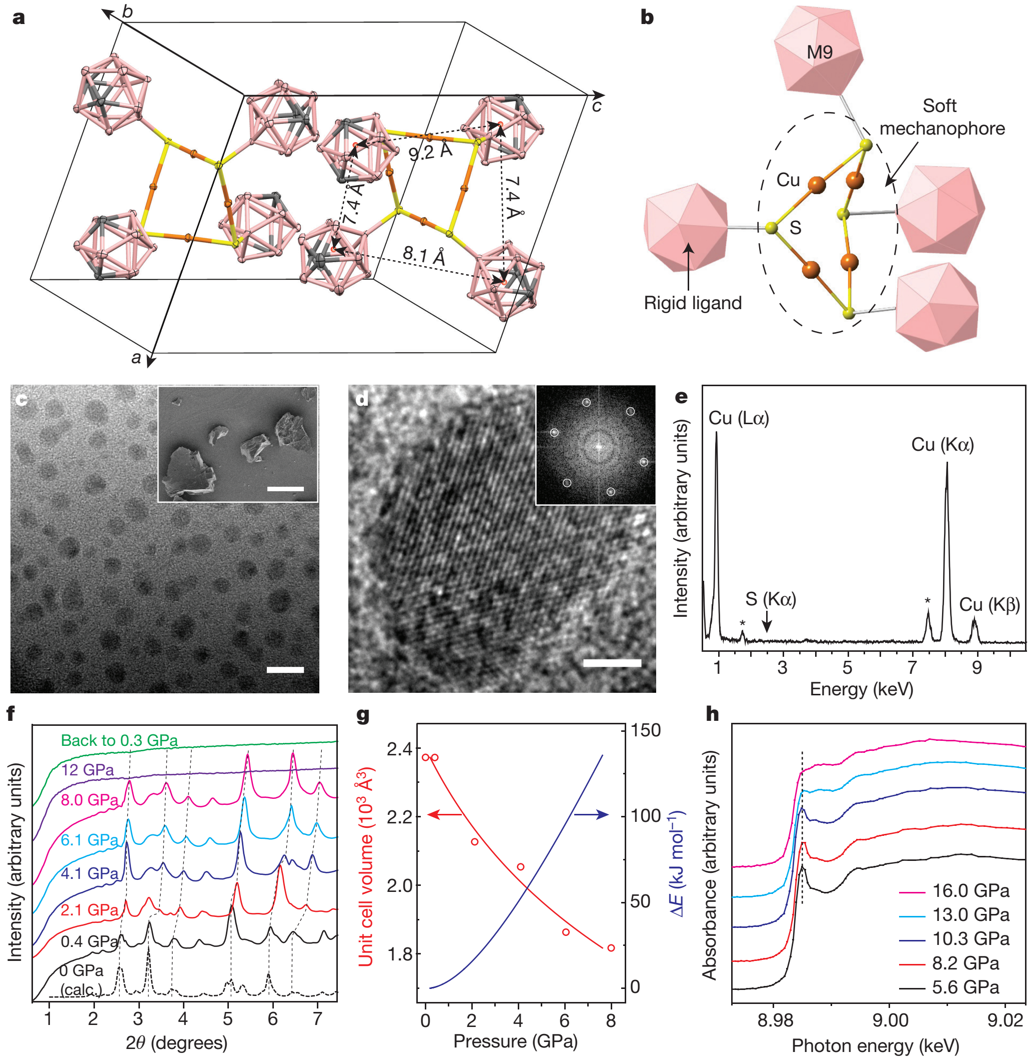

Figure 1 | Redox reaction in Cu-S-M9 under hydrostatic pressure. **a**, Unit cell of Cu-S-M9. Atoms are represented by their thermal ellipsoids at the 50% probability level. Copper, sulfur, carbon and boron atoms are represented by red, yellow, grey and pink ellipsoids, respectively. Hydrogen atoms and interstitial solvent (toluene) molecules are omitted for clarity. **b**, Cu-S-M9 molecule showing the Cu_4S_4 mechanophore surrounded by M9 ligands, represented by polyhedra. **c**, TEM image of nanoclusters formed after compression to 12 GPa. Scale bar, 100 nm. Inset, scanning electron microscopy image of Cu-S-M9 crystals before compression. Scale bar, 50 μm. **d**, High-resolution TEM image of a single copper nanocluster. Scale bar, 2 nm. Inset, Fourier transform pattern. **e**, EDS of the clusters shown in **c** and **d**. The arrow points to the position of the S K-edge. The asterisks mark background signals of Ni and Si. **f**, *In situ* XRD patterns of Cu-S-M9 from 0.4 GPa to 12 GPa and back to 0.3 GPa. $\lambda = 0.4959$ Å. The bottom dashed line shows the ambient XRD pattern calculated from its crystal structure. The vertical dashed lines mark the positions of six selected peaks used to determine the lattice parameters (see Methods and Supplementary Table 5). **g**, Unit cell volume (red, left axis) and total energy change (blue, right axis) as functions of pressure. Open circles and solid lines represent the experimentally derived data and the fitting calculation using a third-order Birch–Murnaghan equation of state, respectively. **h**, *In situ* XAS at different pressures. The dashed line marks the position of the Cu(I) peak.

the characteristic Cu(I) peak (8,985 eV, ref. 23) decreases at 8–13 GPa (Fig. 1h), consistent with the pressure range of structural transformation. Although the decreased Cu(I) peak intensity can be attributed to formation of Cu(0) or Cu(II), *ex situ* X-ray photoelectron spectroscopy data (Extended Data Fig. 4) exclude the formation of Cu(II). These results show that pressure higher than 8 GPa drives the reduction of Cu(I) to form metallic Cu(0).

DFT computations show that the hydrostatic pressure leads to relative motion of the M9 ligands, which in turn change the bonding in the Cu_4S_4 core. We computed the equilibrium structures of Cu-S-M9 at 2–12 GPa (Fig. 2a–d) using the generalized gradient approximation (GGA) level of DFT. The GGA provided a good representation of the system under pressure even without inclusion of dispersion interactions (Methods and Extended Data Fig. 7).

First, the DFT results confirm the large compressibility difference between the Cu_4S_4 mechanophore and M9 ligands. The bond lengths in M9 decrease slightly (<0.1 Å) between ambient pressure and 12 GPa (black and yellow, Fig. 2e), reflecting the rigidity of the ligand in this pressure range. The compression decreases the spacing between the M9 ligands. For example, the distance between the adjacent M9$_1$ and M9$_2$ ligands decreases by >1 Å (red, Fig. 2e). Correspondingly, the distance between the two sulfur atoms connected with M9$_1$ and M9$_2$, S1 and S2, decreases by 0.8 Å (blue, Fig. 2e). These changes are at least one order of magnitude larger than the bond length changes within M9 groups, demonstrating the large compressibility difference between the mechanophore and the ligands. The S2–S3 and M9$_2$–M9$_3$ distances show similar changes (Extended Data Fig. 8).

Second, the computed structures show that the Cu_4S_4 core is anisotropically deformed by the hydrostatic pressure. The system accommodates the reduced S1–S2 distance by bending the S1–Cu1–S2 bond angle from 176° at ambient pressure to 104° at 12 GPa (green, Fig. 2e). The S2–Cu2–S3 bond angle shows the same trend, while

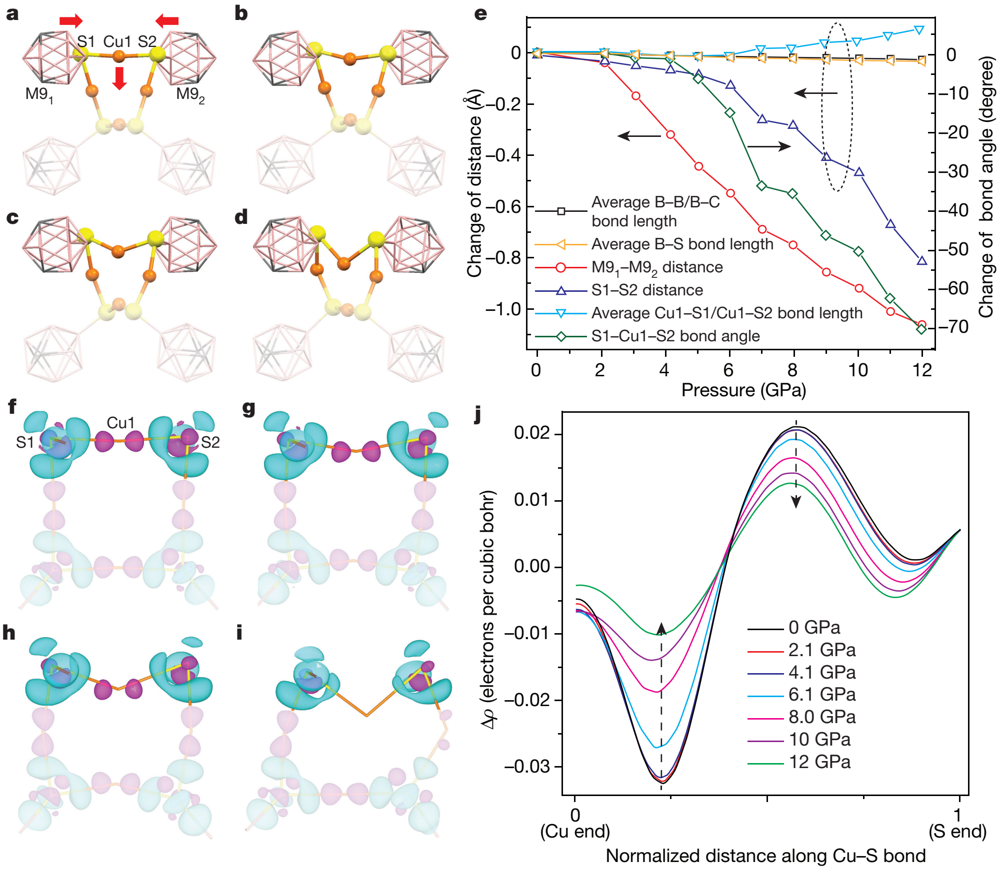

Figure 2 | Modelling the atomic and electronic structures of Cu-S-M9. **a**–**d**, DFT-computed structures of Cu-S-M9 at 2.1 GPa (**a**), 6.1 GPa (**b**), 8.0 GPa (**c**) and 12 GPa (**d**). The red arrows denote the directions of relative motion of copper, sulfur and M9. **e**, Changes of distances (left axis) and bond angle (right axis) as functions of pressure. **f**–**i**, Isosurfaces of $\Delta\rho$ at 2.1 GPa (**f**), 6.1 GPa (**g**), 8.0 GPa (**h**) and 12 GPa (**i**). Cyan and magenta represent isovalues of ± 0.012 electrons per cubic bohr, respectively. The carboranes are omitted for clarity. **j**, Averaged line profiles of $\Delta\rho$ along Cu1–S1 and Cu1–S2 bonds at different pressures. The dashed arrows mark the positions of $\Delta\rho$ maxima near sulfur and minima near copper, with the arrow pointing in the direction of increasing pressure.

changes in the two other S–Cu–S bond angles are smaller (Extended Data Fig. 8).

Interestingly, the bending of the S1–Cu1–S2 angle substantially stretches the Cu1–S1 and Cu1–S2 bonds by up to 4% between 7 GPa and 12 GPa (cyan, Fig. 2e), suggesting weakening of the bond strength in this pressure range. The onset pressure is within 1 GPa of the reaction onset pressure observed by *in situ* XRD and XAS. This is due to emergence of nodal planes in the highest occupied molecular orbital (HOMO) across the Cu–S bonds (Extended Data Fig. 9), transforming the HOMO into an antibonding orbital. We note that although equilibrium structures can be computed up to 12 GPa, experimentally the system is sufficiently destabilized above 8 GPa, and reaction takes place spontaneously at room temperature.

The anisotropic deformation of the mechanophore leads to electron transfer from sulfur to copper. Figure 2f–i depicts the electron density difference ($\Delta\rho$), defined as the electron density of the molecule minus the superposition of electron densities of isolated atoms, from ambient pressure to 12 GPa. At ambient pressure, the negative (magenta) and positive (cyan) $\Delta\rho$ near Cu1 and S1/S2 is consistent with the valence of the elements (+1 for Cu and −2 for S). As the pressure increases, both the negative and positive $\Delta\rho$ isosurfaces near Cu1 and S1/S2 shrink in size. At 12 GPa, the electron density near Cu1 is within 0.01 electron per cubic bohr of the electron density of elemental Cu(0). The minima and maxima of $\Delta\rho$ along the Cu–S bonds decrease by 70% and 40% respectively from ambient pressure to 12 GPa (Fig. 2j). These computational results indicate that as the S–Cu–S bond angle is bent, electron density is transferred from S to Cu, resulting in the reduction of Cu(I), consistent with the experimental observation of elemental copper nanoclusters.

The redox reaction in Cu-S-M9 demonstrates that the relative motion of M9 ligands enables anisotropic deformation and reactivity of the Cu–S mechanophore. In contrast, in metal–organic chalcogenides (MOCs) where the rigid ligands contact each other, the relative motion of the ligands is sterically hindered, prohibiting the deformation and reactivity of the metal–chalcogen mechanophore. We demonstrate this 'steric blockage' scenario (Extended Data Fig. 1) in copper(I) adamantane-1-thiolate (Cu-S-Ada, Fig. 3a). The mechanophore, a Cu–S nanowire with a three-atom cross-section, is surrounded by a ligand shell consisting of adamantyl groups. We note that unlike Cu-S-M9, here the adamantyl groups are in van der Waals contact[16,24].

In this case, the sterically hindered ligand shell impedes relative movement of the adamantyl groups and deformation of the Cu–S mechanophore. Equilibrium structures computed by DFT (Fig. 3b) shows that the adamantyl groups are rigid from ambient pressure to 20 GPa, with <0.01 Å change of the average C–C bond lengths (black, Fig. 3c). During the compression process, the decrease of adjacent adamantyl distances (red, Fig. 3c) is 40% less than the maximal M9–M9 distance change in Cu-S-M9, indicating much smaller relative motion. Correspondingly, the average S–S distance and S–Cu–S bond angle changes by about 3% and 13% respectively from ambient pressure to 20 GPa (blue and green, Fig. 3c), substantially smaller than the changes in Cu-S-M9 (about 20% and 40%, respectively, from ambient pressure to 12 GPa). The average Cu–S bond length slightly decreases (cyan, Fig. 3c) at 20 GPa, in clear contrast to the stretching of Cu–S bonds in Cu-S-M9 at 12 GPa and suggesting no bond weakening.

DFT computations indicate a much smaller electron density shift in Cu-S-Ada than in Cu-S-M9. The positive and negative electron

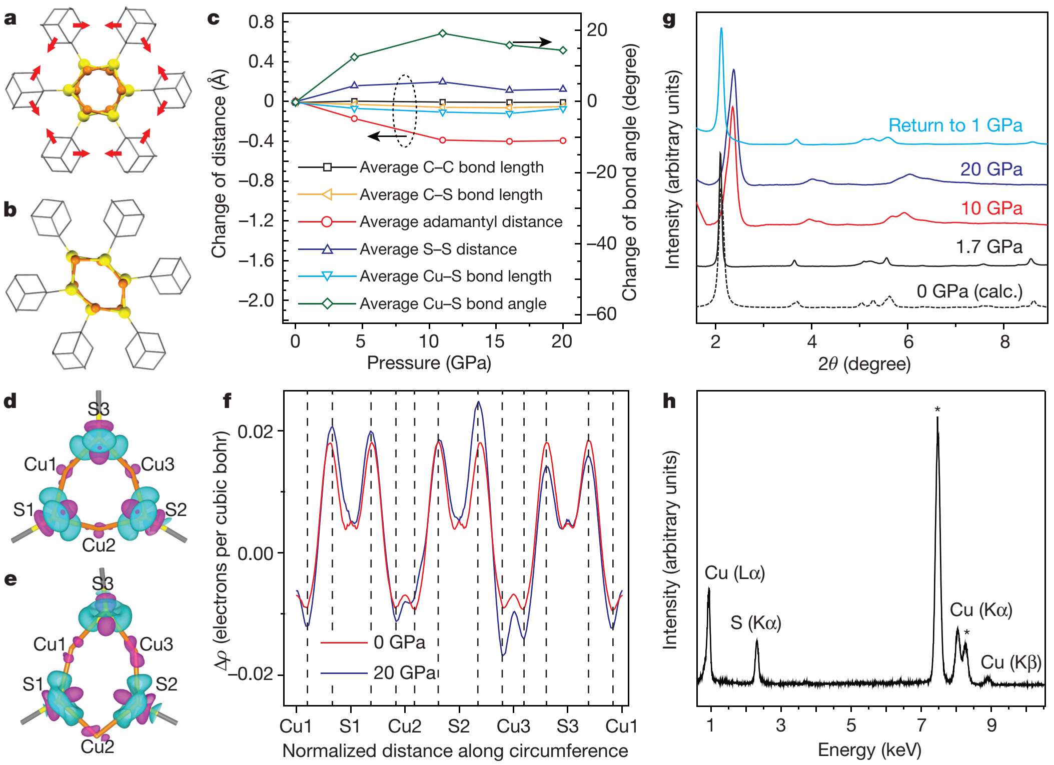

Figure 3 | Sterically impeded reactivity in Cu-S-Ada. a, Ambient-pressure structure of Cu-S-Ada, viewed along the nanowire elongation direction. Red arrows denote the direction of motion for the adamantyl groups under pressure. Copper and sulfur atoms are represented by red and yellow spheres, and the adamantyl groups are represented by the capped stick model. **b**, DFT-computed structure at 20 GPa. **c**, Changes of distances (left axis) and bond angle (right axis) as functions of pressure. **d**, **e**, $\Delta\rho$ isosurfaces at ambient pressure (**d**) and at 20 GPa (**e**). Cyan and magenta represent isovalues of ±0.009 electrons per cubic bohr, respectively. Adamantyl groups are omitted for clarity. **f**, $\Delta\rho$ line profiles along Cu–S bonds on the circumference of the Cu–S nanowire core. The dashed lines mark the positions of $\Delta\rho$ minima near copper atoms and maxima near sulfur atoms. **g**, *In situ* XRD from 1.7 GPa to 20 GPa and back to 1 GPa. $\lambda = 0.4959$ Å. The bottom dashed line shows the XRD pattern calculated from its ambient crystal structure. **h**, EDS of Cu-S-Ada after compression to 20 GPa. The asterisk marks the Ni peak from the TEM grid.

density differences near sulfur and copper atoms persist from ambient pressure up to 20 GPa (Fig. 3d and e). Figure 3f depicts the line profile of $\Delta\rho$ along the Cu–S bonds. It can be seen that the $\Delta\rho$ maxima near S3 decrease by 0.004 electrons per cubic bohr from ambient pressure to 20 GPa, much smaller than the change (about 40%) in Cu-S-M9. On the other hand, the absolute values of $\Delta\rho$ maxima/minima near the other S and Cu atoms increase by up to 0.008 electrons per cubic bohr, indicating an electron density shift from S to Cu in contrast to the S-to-Cu electron transfer observed in Cu-S-M9. These computational results suggest that the reduction of Cu(I) by sulfur, observed in Cu-S-M9, would be hindered in Cu-S-Ada, and we predict that Cu-S-Ada remains mechanochemically inert up to 20 GPa.

This prediction was verified by experiments. *In situ* XRD (Fig. 3g) shows that the diffraction peaks attributed to Cu-S-Ada shift smoothly from ambient pressure to 20 GPa, indicating no amorphization in this pressure range. Upon releasing the pressure, the ambient XRD pattern is fully recovered, showing that the deformation is elastic. EDS of a sample compressed to 20 GPa (Fig. 3h) reveals both copper and sulfur, consistent with the composition of the pristine Cu-S-Ada[16]. The nanowire morphology of the sample is also preserved after compression (Extended Data Fig. 10). No elemental copper clusters could be observed by TEM. These computational and experimental results corroborate that the sterically hindered adamantyl ligand shell in Cu-S-Ada impedes the anisotropic deformation and redox reaction in the Cu–S core. Importantly, the steric control of reactivity does not exist in the thermochemistry of these compounds, as both Cu-S-M9 and Cu-S-Ada yield cuprous sulfide under the same pyrolysis conditions (Extended Data Fig. 5).

The mechanochemistry based on relative motion of rigid ligands can be extended to other molecular architectures. We examined the mechano-reactivity of two different one-dimensional silver diamondoidthiolate structures under hydrostatic pressure. The model systems consisted of two chemically similar, yet sterically different compounds, silver(I) diamantane-1-thiolate (Ag-S-*m*Dia, where *m* denotes the medial position of the thiol group) and silver(I) adamantane-1-thiolate (Ag-S-Ada)[16]. Both structures have two single-atom Ag-S chains packed together via van der Waals interaction and surrounded by diamondoid sidegroups (Fig. 4a and b, Supplementary Table 1, Extended Data Fig. 2). In Ag-S-*m*Dia the two diamantyl groups reside on the same side of the Ag–S chain, adopting a *cis* configuration (Fig. 4a). In contrast, in Ag-S-Ada the two adamantyl groups reside on the opposite side of the Ag-S chain, taking up a *trans* configuration (Fig. 4b). We postulate that in the *cis* configuration, the relative sliding of the two Ag–S chains may occur perpendicular to the chain elongation direction (red arrows, Fig. 4a). In the *trans* configuration steric repulsion between adamantyl groups in adjacent chains would impede relative motion.

DFT computations show that the Ag–S mechanophore in Ag-S-*m*Dia sustains much larger deformation than Ag-S-Ada under hydrostatic pressure. The chain alignment angle, defined by sulfur atoms in the two adjacent chains as shown in Fig. 4a, increases by >10% in Ag-S-*m*Dia from ambient pressure to 20 GPa (blue, Fig. 4c). In contrast, the chain alignment angle in Ag-S-Ada decreases by approximately 2% in the same pressure range (red, Fig. 4c). Instead of shearing the mechanophore, the Ag-S-Ada system absorbs the stress by buckling the Ag–S chains.

This displacement in Ag-S-*m*Dia chains results in an electron density shift towards silver. At ambient pressure, negative and positive $\Delta\rho$ isosurfaces exist near all Ag and S atoms of Ag-S-*m*Dia (upper panel of Fig. 4d), consistent with their respective valences (+1 for Ag and −2 for S). At 20 GPa, however, the $\Delta\rho$ near half of the Ag atoms (Ag1 and Ag2, lower panel of Fig. 4d) decreases below 0.01 electrons

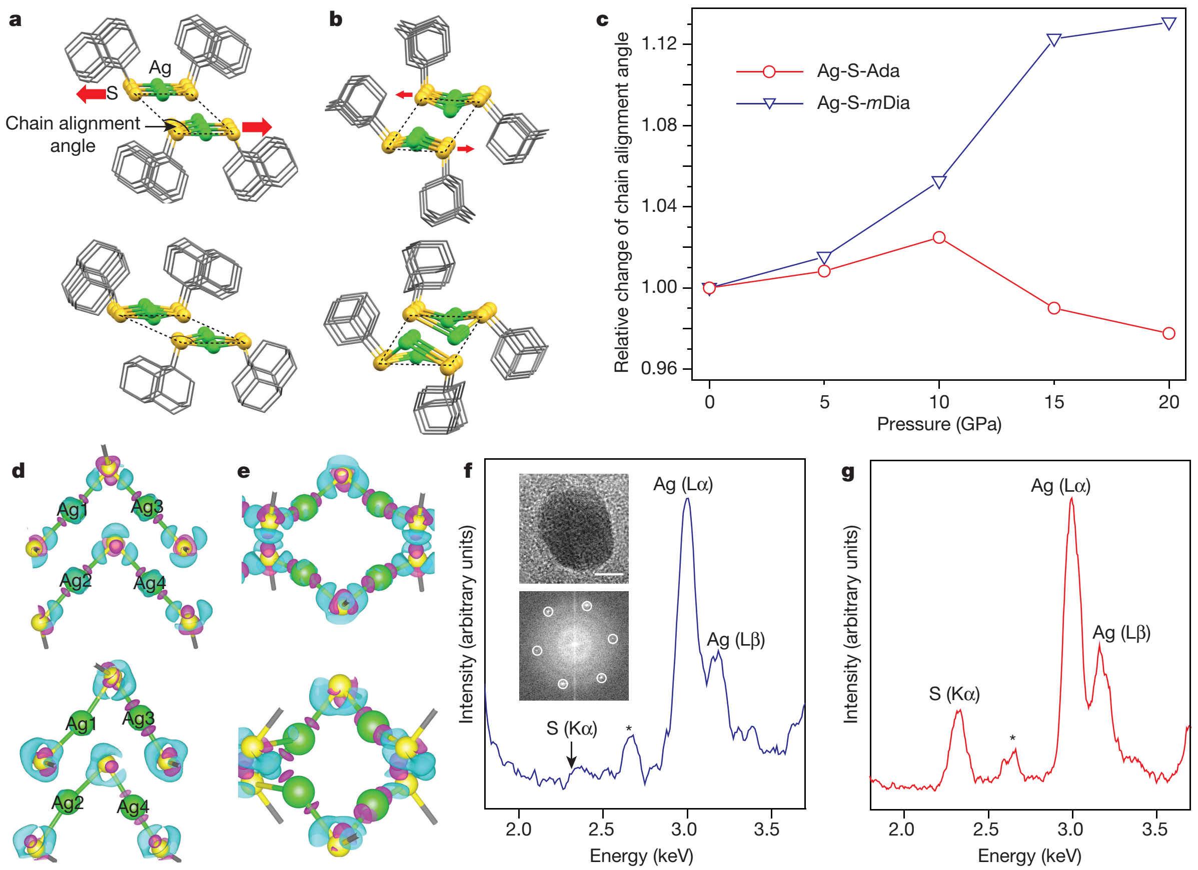

Figure 4 | Sterically controlled deformation and reactivity in one-dimensional structures. a, **b**, Atomic structures of Ag-S-*m*Dia (**a**) and Ag-S-Ada (**b**) at ambient pressure (top) and 20 GPa (bottom). Ambient-pressure and high-pressure structures are determined by single-crystal XRD and DFT computation, respectively. The structures are viewed along the chain elongation directions. Silver and sulfur are represented by green and yellow spheres, and the diamondoids are represented by capped stick models. The red arrows denote the directions of motion for the two adjacent Ag–S chains. **c**, Relative changes of chain alignment angles as functions of pressure for Ag-S-Ada and Ag-S-*m*Dia. **d**, **e**, $\Delta\rho$ isosurfaces for Ag-S-*m*Dia (**d**) and Ag-S-Ada (**e**) at ambient (top) and 20 GPa (bottom) pressures. Cyan and magenta represent isovalues of ± 0.01 electrons per cubic bohr, respectively. **f**, EDS of Ag-S-*m*Dia after 20 GPa compression. Top inset, TEM image of a silver nanocluster. Scale bar, 5 nm. Bottom inset, Fourier transform pattern of the TEM image. **g**, EDS of Ag-S-Ada after 20 GPa compression. The asterisks in **f** and **g** mark background Cl signals from solvent residue.

per cubic bohr. The magnitude of this decrease in $\Delta\rho$ near Ag1 and Ag2 is comparable to that near Cu1 of Cu-S-M9 at 12 GPa, and suggests the reduction of Ag(I) to Ag(0) at 20 GPa. On the other hand, although the Ag–S chain in Ag-S-Ada is buckled by hydrostatic compression, the negative $\Delta\rho$ adjacent to all Ag atoms persists from ambient pressure to 20 GPa (Fig. 4e), suggesting that the redox reaction is blocked within this pressure range.

The different mechano-reactivity predicted by DFT is confirmed by the experiments. TEM of a Ag-S-*m*Dia sample after compression to 20 GPa (upper inset of Fig. 4f) reveals crystalline nanoclusters with lattice spacing of 2.4 Å, consistent with the [111] spacing of silver. EDS (Fig. 4f) shows that these clusters consist exclusively of silver and are free of sulfur, thus confirming the formation of elemental silver by hydrostatic compression. In contrast, no silver clusters can be observed in Ag-S-Ada samples after compression to 20 GPa. Although large particles are observed (Extended Data Fig. 10), these particles have no identifiable lattice under TEM. Furthermore, EDS reveals that these particles consist of both silver and sulfur (Fig. 4g), consistent with the composition of pristine Ag-S-Ada. We conclude that although the 20 GPa hydrostatic pressure changes the morphology (from nanowire to particles), and possibly the crystallinity, there is no evidence of a redox reaction in this compound. The computational and experimental results demonstrate that steric effects control the deformation and associated reactivity in one-dimensional MOCs, implementing the molecular anvil and steric blockage scenarios with a different reaction mechanism from the bond angle bending in Cu-S-M9.

The molecular anvils offer an atomic-efficient design of mechanochemical systems with a ligand-to-mechanophore atomic ratio of the order of ten. In contrast, polymeric mechanochemical systems require long chains with about a thousand repeating units supporting the mechanophore[25], with a polymer-to-mechanophore atomic ratio of at least one hundred. These results suggest that rigid and sterically bulky functional groups, which are widely explored in conventional organic synthesis as protecting and directing groups, might also be readily adopted for mechanochemistry, opening new methods towards highly specific mechanosynthesis.

Online Content Methods, along with any additional Extended Data display items and Source Data, are available in the online version of the paper; references unique to these sections appear only in the online paper.

Received 5 September 2017; accepted 8 January 2018.

1. Gilman, J. J. Mechanochemistry. *Science* **274,** 65–66 (1996).
2. Caruso, M. M. *et al.* Mechanically-induced chemical changes in polymeric materials. *Chem. Rev.* **109,** 5755–5798 (2009).
3. Hickenboth, C. R. *et al.* Biasing reaction pathways with mechanical force. *Nature* **446,** 423–427 (2007).
4. May, P. A. *et al.* Polymer mechanochemistry: techniques to generate molecular force via elongational flows. *Chem. Soc. Rev.* **42,** 7497–7506 (2013).
5. Huang, Z. & Boulatov, R. Chemomechanics: chemical kinetics for multiscale phenomena. *Chem. Soc. Rev.* **40,** 2359–2384 (2011).
6. Diesendruck, C. E. *et al.* Mechanically triggered heterolytic unzipping of a low-ceiling-temperature polymer. *Nat. Chem.* **6,** 623–628 (2014).
7. Piermattei, A., Karthikeyan, S. & Sijbesma, R. P. Activating catalysts with mechanical force. *Nat. Chem.* **1,** 133–137 (2009).

8. Klukovich, H. M. *et al.* A backbone lever-arm effect enhances polymer mechanochemistry. *Nat. Chem.* **5,** 110–114 (2013).
9. Chen, Y. *et al.* Mechanically induced chemiluminescence from polymers incorporating a 1,2-dioxetane unit in the main chain. *Nat. Chem.* **4,** 559–562 (2012).
10. Davis, D. A. *et al.* Force-induced activation of covalent bonds in mechanoresponsive polymeric materials. *Nature* **459,** 68–72 (2009).
11. Wang, J., Kouznetsova, T. B. & Craig, S. L. Single-molecule observation of a mechanically activated *cis*-to-*trans* cyclopropane isomerization. *J. Am. Chem. Soc.* **138,** 10410–10412 (2016).
12. Chen, Z. *et al.* Mechanochemical unzipping of insulating polyladderene to semiconducting polyacetylene. *Science* **357,** 475–479 (2017).
13. Li, W. & Gräter, F. Atomistic evidence of how force dynamically regulates thiol/disulfide exchange. *J. Am. Chem. Soc.* **132,** 16790–16795 (2010).
14. Dopieralski, P. *et al.* The Janus-faced role of external forces in mechanochemical disulfide bond cleavage. *Nat. Chem.* **5,** 685–691 (2013).
15. Akbulatov, S. *et al.* Experimentally realized mechanochemistry distinct from force-accelerated scission of loaded bonds. *Science* **357,** 299–303 (2017).
16. Yan, H. *et al.* Hybrid metal–organic chalcogenide nanowires with electrically conductive inorganic core through diamondoid-directed assembly. *Nat. Mater.* **16,** 349 (2017).
17. Gamba, Z. & Powell, B. M. The condensed phases of carboranes. *J. Chem. Phys.* **105,** 2436 (1996).
18. Schwertfeger, H., Fokin, A. A. & Schreiner, P. R. Diamonds are a chemist's best friend: diamondoid chemistry beyond adamantane. *Angew. Chem. Int. Ed.* **47,** 1022–1036 (2008).
19. Gunawan, M. A. *et al.* Diamondoids: functionalization and subsequent applications of perfectly defined molecular cage hydrocarbons. *New J. Chem.* **38,** 28–41 (2014).
20. Castner, D. G., Hinds, K. & Grainger, D. W. X-ray photoelectron spectroscopy sulfur 2p study of organic thiol and disulfide binding interactions with gold surfaces. *Langmuir* **12,** 5083–5086 (1996).
21. Schneider, S., Dzudza, A., Raudaschl-Sieber, G. & Marks, T. J. Copper(I) *tert*-butylthiolato clusters as single-source precursors for high-quality chalcocite thin films: precursor chemistry in solution and the solid state. *Chem. Mater.* **19,** 2768–2779 (2007).
22. Birch, F. Finite elastic strain of cubic crystals. *Phys. Rev.* **71,** 809–824 (1947).
23. Jang, Y. J. *et al.* Tree branch-shaped cupric oxide for highly effective photoelectrochemical water reduction. *Nanoscale* **7,** 7624–7631 (2015).
24. Nowacki, W. Die Krystallstruktur von Adamantan (symm. *Tri-cyclo-decan). Helv. Chim. Acta* **28,** 1233–1242 (1945).
25. May, P. A. *et al.* Is molecular weight or degree of polymerization a better descriptor of ultrasound-induced mechanochemical transduction? *ACS Macro Lett.* **5,** 177–180 (2016).

Supplementary Information is available in the online version of the paper.

Acknowledgements We thank C. Beavers, J. Yan and S. Teat from the Advanced Light Source for help with XRD measurements, and C. Park and D. Popov from the Advanced Photon Source for XAS measurements. This work was supported by the Department of Energy, Office of Basic Energy Sciences, Division of Materials Science and Engineering, under contracts DE-AC02-76SF00515 and DE-FG02-06ER46262. D.P. acknowledges support from Hong Kong Research Grants Council (project number ECS-26305017), the National Natural Science Foundation of China (project number 11774072) and the Alfred P. Sloan Foundation through the Deep Carbon Observatory. D.S.-I. acknowledges support from PAPIIT IA203116/27 and CONACYT FC-2015-2/829. This research used resources of the Advanced Light Source, which is a US Department of Energy (DOE) Office of Science User Facility under contract DE-AC02-05CH11231. This research also used resources of the Advanced Photon Source, a DOE Office of Science User Facility operated for the DOE Office of Science by Argonne National Laboratory under contract DE-AC02-06CH11357. Portions of this work were performed at the Stanford Nano Shared Facilities, supported by the National Science Foundation under award ECCS-1542152. The computational work used resources at the Stanford Research Computing Center, the Research Computing Center at the University of Chicago, and the Deep Carbon Observatory computer cluster.

Author Contributions H.Y., W.L.M., Z.-X.S. and N.A.M. conceived the idea. H.Y., J.N.H. and D.S.-I. synthesized the crystals and solved their structures. H.Y., F.Y. and Y.L. carried out the high-pressure experiments. H.Y., D.P. and G.G. performed the DFT computations. H.Y. and F.H.L. performed the *ex situ* characterizations. J.E.P.D., R.M.K.C., B.A.T., A.A.F. and P.R.S. provided the diamondoids and synthesized their derivatives. H.Y. and N.A.M. wrote the paper. All authors contributed to the discussion and revision of the paper.

Author Information Reprints and permissions information is available at www.nature.com/reprints. The authors declare no competing financial interests. Readers are welcome to comment on the online version of the paper. Publisher's note: Springer Nature remains neutral with regard to jurisdictional claims in published maps and institutional affiliations. Correspondence and requests for materials should be addressed to N.A.M. (nmelosh@stanford.edu).

Reviewer Information *Nature* thanks D. Braga, S. James and L. Yan for their contribution to the peer review of this work.

METHODS

Synthesis and structural determination of MOCs. All commercially available chemicals were purchased from Sigma Aldrich and used without further purification. Anhydrous chemicals were used when possible. Synthesis of Cu-S-Ada, Ag-S-Ada and Ag-S-*m*Dia was described previously[16]. Cu-S-M9 was synthesized in an argon-filled glove box. 20 mM solutions of *m*-carborane-9-thiol in toluene and copper sulfate in ethylene glycol were layered in a glass vial, with 1:1 volumetric ratio and the toluene phase on top. The mixture was heated at 70 °C for a week. Upon cooling to room temperature, colourless crystals appear at the toluene/ethylene glycol interface. The crystals were harvested by vacuum filtration, washed with ethanol and dried under vacuum.

Single-crystal XRD of Cu-S-M9 and Ag-S-Ada was performed using a Bruker D8 Venture diffractometer, equipped with a MoK$_\alpha$ source (wavelength $\lambda = 0.7107$ Å) and a Photon 100 complementary metal-oxide-semiconductor detector. Single-crystal XRD of Ag-S-*m*Dia was measured with synchrotron radiation ($\lambda = 0.7749$ Å) at Beamline 11.3.1, Advanced Light Source, Lawrence Berkeley National Laboratory, with a Bruker D8 diffractometer and a Bruker AXS APEXII CCD detector. Crystals were coated with Paratone-N oil, attached to Kapton loops, and mounted on the diffractometer. Frames were collected using ω and/or ψ scans and the unit-cell parameters were refined against all data. Data were integrated and corrected for Lorentz and polarization factors, as well as the absorption effects using SAINT 8.27b and SADABS software integrated in the APEX2 suite[26]. Space-group assignments were based upon systematic absences, *E*-statistics, agreement factors for equivalent reflections, and successful refinement of the structure. The structures were solved by direct methods and expanded through successive difference Fourier maps using SHELXS-97. They were refined against all data using SHELXTL and OLEX2 software[27–29]. Hydrogen atoms were inserted at idealized positions and refined using a riding model with an isotropic thermal parameter 1.2 times that of the attached atom. Thermal parameters for all non-hydrogen atoms were refined anisotropically. Details of the data quality and a summary of the residual values of the refinements are listed in Supplementary Table 1.

High pressure experiments. Compression and *in situ* XRD/XAS were performed using a diamond anvil cell with a 500-μm diamond culet. The sample chamber was created by drilling a 150-μm hole in a pre-indented stainless steel gasket. Two types of experiments were performed. In the first, the chamber was filled with approximately a few thousand crystals in the size range 1–10 μm, and no pressure medium was used. In the second scenario, a single crystal with size approximately 100 μm was loaded in the chamber together with neon as the pressure medium. In both cases we observed formation of elemental copper after compression beyond 12 GPa. The pressure was monitored with the photoluminescence of a 5-μm ruby ball loaded together with the samples. Pressure was increased and decreased gradually in steps of a few hundred megapascals, and roughly at a rate of 1 GPa min^{-1}. Pressure values reported throughout the paper have 5% uncertainty[30].

In situ powder XRD was performed at Beamline 12.2.2, Advanced Light Source, Lawrence Berkeley National Laboratory. A monochromatic beam ($\lambda = 0.4959$ Å) was used. Samples were measured with the Debye–Scherrer geometry. The Debye rings were integrated using the FIT2D software[31]. To derive the lattice parameters from the diffraction patterns, the lattice spacings corresponding to six diffraction peaks with known Miller indices (vertical dashed lines in Fig. 1f, see also Supplementary Table 5) were calculated at different pressures. Note that in triclinic crystals

$$\frac{1}{d_{hkl}^2} = \frac{1}{V^2}(S_{11}h^2 + S_{22}k^2 + S_{33}l^2 + 2S_{12}hk + 2S_{23}kl + 2S_{13}hl)$$

where *d* is the lattice spacing, *hkl* is the Miller index, *a*, *b*, *c*, α, β and γ are the lattice parameters, *V* is the unit cell volume, and

$$S_{11} = b^2c^2\sin^2\alpha$$

$$S_{22} = a^2c^2\sin^2\beta$$

$$S_{33} = a^2b^2\sin^2\gamma$$

$$S_{12} = abc^2(\cos\alpha\cos\beta - \cos\gamma)$$

$$S_{23} = a^2bc(\cos\beta\cos\gamma - \cos\alpha)$$

$$S_{13} = ab^2c(\cos\alpha\cos\gamma - \cos\beta)$$

The lattice parameters can thus be found by numerically solving the nonlinear equation sets.

High pressure XAS experiments were performed at Beamline 16-BMD HPCAT, Advanced Photon Source, Argonne National Laboratory. Monochromatic X-rays focused by Kirkpatrick–Baez mirrors were directed through a symmetric diamond anvil cell. The scattered X-ray was then energy-selected by an analyser and collected by the detector. The entire edge was scanned from 8,970 eV to 9,025 eV with a step size of 0.25 eV. The pre-edge was scanned from 8,980 eV to 8,990 eV with a step size of 0.1 eV.

***Ex situ* characterizations.** TEM imaging and EDS were collected on an FEI Tecnai F20 system operating at 200-kV accelerating voltage. To prepare the TEM samples, the metal gasket containing the post-compression material was unloaded from the diamond anvil cell and sonicated in isopropanol. The supernate was drop-cast on a nickel TEM grid (Ted Pella). The TEM grid was then rinsed in chloroform and dried in vacuum. We note that the sonication or imaging process does not produce metal nanoclusters (Extended Data Fig. 3).

Scanning electron microscopy images were acquired with an FEI Magellan system operating at 2-kV acceleration voltage. Sample powders were gently pressed onto a degenerately doped silicon wafer, and sputter-coated with about 5-nm-thick Au/Pd before imaging.

X-ray photoelectron spectroscopy was measured on a PHI Versaprobe system with monochromated AlK$_\alpha$ source (1,486 eV). Pristine sample powders were pressed onto a degenerately doped silicon wafer. Compressed samples were characterized in the gasket.

Ex situ XRD was performed on a Bruker D8 Venture system equipped with a MoK$_\alpha$ source ($\lambda = 0.7107$ Å) and a complementary metal-oxide-semiconductor detector. Powder samples were filled into borosilicate capillary tubes and measured with the Debye–Scherrer geometry. The Debye rings were integrated using the APEX3 software suite.

DFT computations. DFT computations were performed with the plane-wave basis set, the Perdew–Burke–Ernzerhof (PBE) exchange-correlation functional[32] and the projector augmented wave method, implemented in the Quantum ESPRESSO package[33]. For each pressure, the crystal structure was first optimized using the Broyden–Fletcher–Goldfarb–Shanno (BFGS) algorithm. All atomic positions and lattice parameters were optimized. The kinetic energy cutoffs for wavefunctions and electron density were set at 60 and 240 Rydberg (Ry) for the optimization. The convergence threshold for energy, force and pressure were set to 10^{-4} Ry, 10^{-4} Ry per bohr and 10 MPa, respectively. After convergence of the structural optimization, another single-point calculation with higher cutoffs (80 Ry for wavefunctions and 800 Ry for electron density) was performed to determine the electron density, total energy and stress tensor. The off-diagonal elements of the stress tensors are less than 1% of the diagonal elements (Supplementary Tables 3 and 4), confirming the isotropy of the pressure in these computations. The structural and volumetric data were visualized with Mercury[34] and VESTA[35].

Dispersion interactions are important in determining the ambient structures of MOCs[16]. We included dispersion interactions in the DFT computations of the high-pressure structures using nonlocal exchange-correlation functionals including vdW-DF[36], vdW-DF2[37] and vdW-DF-cx[38]. We found that the unit cell volumes of Cu-S-M9 computed with PBE, vdW-DF and vdW-DF2 all agree reasonably well with experimental data, with less than 5% deviation, while vdW-DF-cx consistently underestimates the unit cell volume, probably owing to overestimation of the dispersion interaction. Furthermore, both PBE and vdW-DF robustly reproduce the key structural changes in Cu-S-M9, that is, shrinkage of the S1–S2 distance, bending of the S1–Cu1–S2 bond angle and elongation of the Cu–S bond beyond 7 GPa (Extended Data Fig. 7). These results indicate that the dispersion interaction does not substantially affect the computed high-pressure structures.

Data availability. Additional data supporting the findings of this study, including raw images, spectra and diffraction patterns, as well as DFT input and output files, are available from the authors. The crystallographic data have been deposited with the Cambridge Crystallographic Data Centre under CCDC-1589700, CCDC-1589701 and CCDC-1589702. These data can be obtained free of charge from The Cambridge Crystallographic Data Centre via www.ccdc.cam.ac.uk/data_request/cif.

26. APEX2, https://www.bruker.com/products/x-ray-diffraction-and-elemental-analysis/single-crystal-x-ray-diffraction/overview/sc-xrd-software/apex3.html (Bruker AXS, 2007).
27. Sheldrick, G. M. *et al.* Crystal structure refinement with *SHELXL*. *Acta Crystallogr. C*. **71,** 3–8 (2015).
28. Sheldrick, G. M. A short history of *SHELX*. *Acta Crystallogr. A* **64,** 112–122 (2008).
29. Dolomanov, O. V. *et al. OLEX2*: a complete structure solution, refinement and analysis program. *J. Appl. Cryst.* **42,** 339–341 (2009).
30. Mao, H.-K. & Mao, W. L. in *Treatise on Geophysics* 231–267 (Elsevier, 2007).
31. Hammersley, A. P. *Internal Report, ESRF98HA01T, FIT2D V9.129 Reference Manual V3.1* (European Synchrotron Radiation Facility (ESRF), 1998).
32. Perdew, J. P., Burke, K. & Ernzerhof, M. Generalized gradient approximation made simple. *Phys. Rev. Lett.* **77,** 3865–3868 (1996).

33. Giannozzi, P. *et al.* QUANTUM ESPRESSO: a modular and open-source software project for quantum simulations of materials. *J. Phys. Condens. Matter* **21,** 395502 (2009).
34. Macrae, C. F. *et al.* Mercury: visualization and analysis of crystal structures. *J. Appl. Cryst.* **39,** 453–457 (2006).
35. Momma, K. & Izumi, F. *VESTA 3* for three-dimensional visualization of crystal, volumetric and morphology data. *J. Appl. Cryst.* **44,** 1272–1276 (2011).
36. Dion, M. *et al.* Van der Waals density functional for general geometries. *Phys. Rev. Lett.* **92,** 246401 (2004).
37. Lee, K. *et al.* Higher-accuracy van der Waals density functional. *Phys. Rev. B* **82,** 081101 (2010).
38. Berland, K. *et al.* Assessment of two hybrid van der Waals density functionals for covalent and non-covalent binding of molecules. *J. Chem. Phys.* **146,** 234106 (2017).

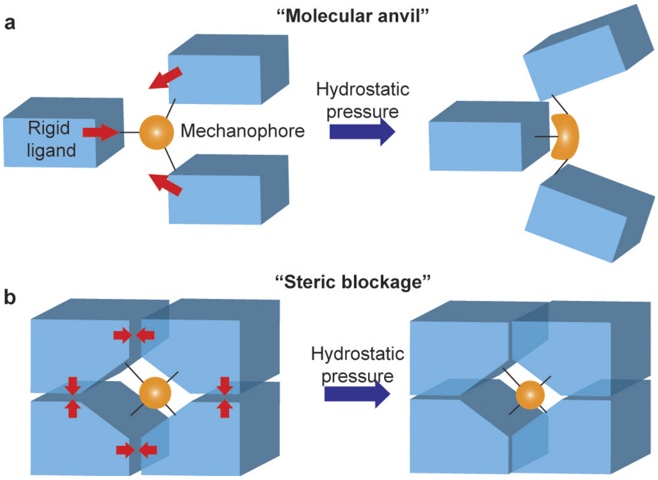

Extended Data Figure 1 | Schematic of the molecular anvil and steric blockage scenarios. a, Relative motions (red arrows) of the rigid ligands under hydrostatic pressure anisotropically deform the mechanophore, leading to reactivity. **b**, Motion of the ligands is blocked by their steric repulsion, protecting the mechanophore from deformation.

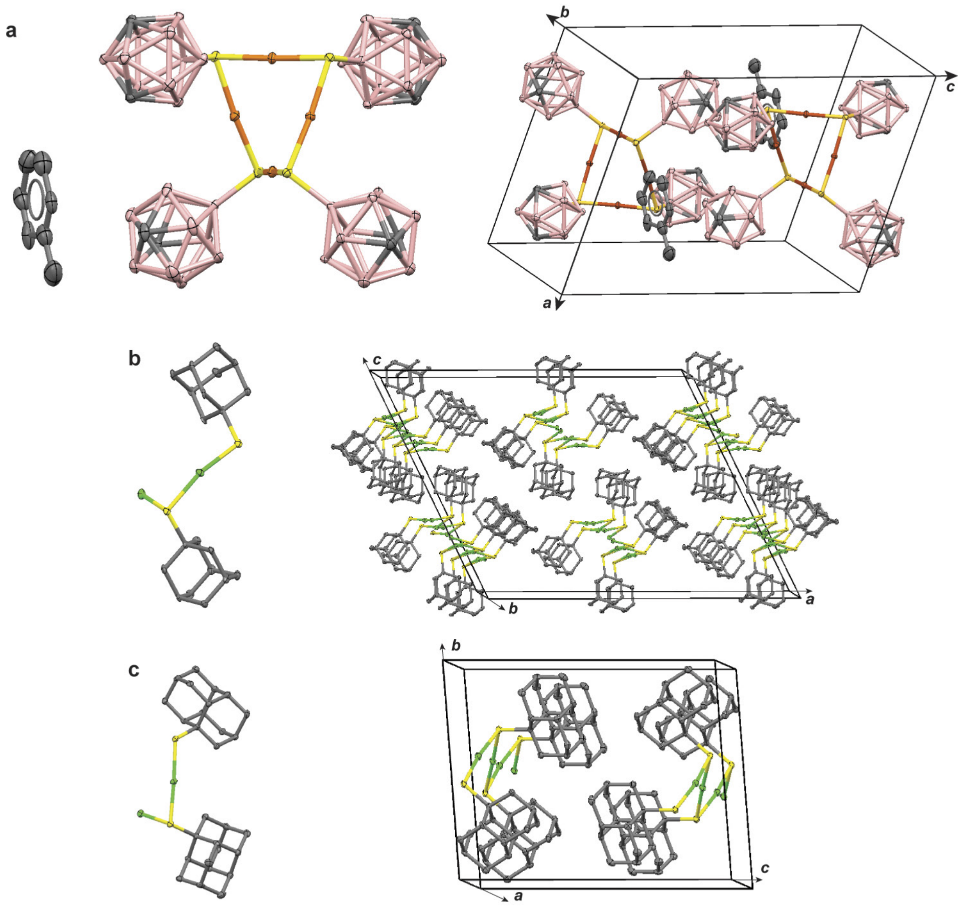

Extended Data Figure 2 | Crystal structures of compounds used in this study. a, Cu-S-M9. **b**, Ag-S-Ada. **c**, Ag-S-*m*Dia. Each panel depicts the asymmetric unit (left) and the unit cell (right). Atoms are represented by their thermal ellipsoids at the 50% probability level. Copper, silver, sulfur, carbon and boron are denoted by red, green, yellow, grey and pink respectively. Hydrogen atoms are omitted for clarity. The toluene molecules (depicted in grey) reside in the interstitial spaces between Cu-S-M9 molecules with a 1:1 molar ratio.

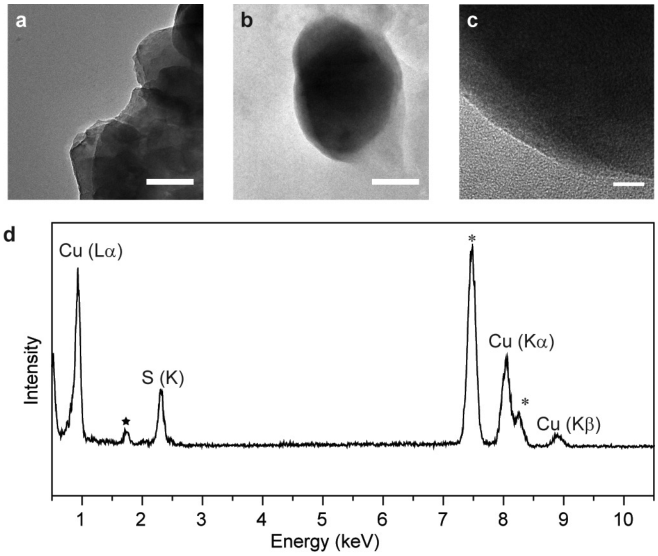

Extended Data Figure 3 | Unreacted Cu-S-M9. a, TEM image of uncompressed Cu-S-M9. **b**, TEM image of Cu-S-M9 after compression to 8 GPa. Scale bars in **a** and **b**, 100 nm. **c**, Zoom-in view of **b**. Scale bar, 10 nm. No inorganic lattice structures are identified in these samples. **d**, Representative EDS of unreacted Cu-S-M9. Both Cu and S peaks can be seen. The asterisks mark Ni peaks originating from the TEM grid. The star marks the position of the Si K-edge, an impurity probably introduced during TEM sample preparation.

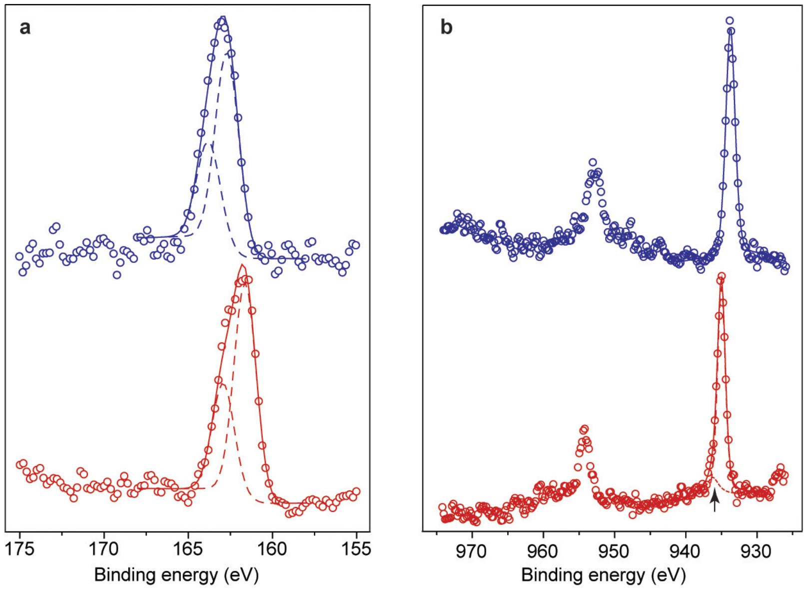

Extended Data Figure 4 | S 2*p* and Cu 2*p* X-ray photoelectron spectroscopy of Cu-S-M9. Red and blue represent uncompressed Cu-S-M9 and sample after compression to 12 GPa, respectively. Discrete dots and solid continuous lines denote experimental data and fitting, respectively. **a**, The S 2*p* spectra are fitted to two Voigt peaks representing $2p_{1/2}$ and $2p_{3/2}$ peaks (dashed lines). The peak position of the uncompressed sample, 162 eV, is characteristic of metal thiolates. The upshift of the binding energy to 163 eV after compression can be attributed to the oxidation of sulfur to form, for example, disulfides. **b**, The Cu 2*p* spectra consist of two peaks, namely $2p_{1/2}$ at about 936 eV and $2p_{3/2}$ at about 954 eV. The absence of satellite peaks excludes the formation of Cu(II) species. Moreover, the $2p_{3/2}$ peak of the uncompressed sample is best fitted by two Voigt peaks (the shoulder peak is denoted by the dashed line and marked by the arrow), characteristic of Cu(I). The $2p_{3/2}$ peak of the compressed sample is best fitted with a single Voigt peak, consistent with Cu(0). These features support the conclusion that copper is in the +1 valence state in the pristine sample, and reduced to the zero valence state upon compression to 12 GPa.

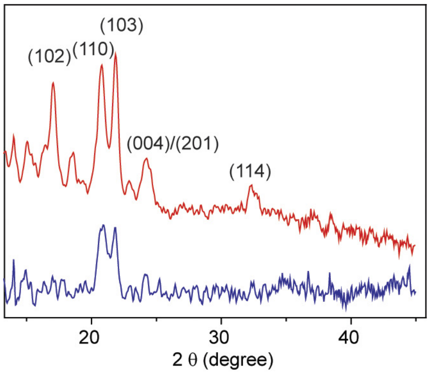

Extended Data Figure 5 | XRD patterns of the pyrolysis products of Cu-S-M9 and Cu-S-Ada. Peaks are registered to β-Cu_2S (chalcocite, PDF Number 00-026-1116). The pyrolysis product of Cu-S-Ada (red) is more crystallized than that of Cu-S-M9 (blue); however, the two strongest peaks, (110) at 20.75° ($d = 1.96$ Å) and (103) at 21.85° ($d = 1.87$ Å) can be clearly seen in both samples. Pyrolysis was carried out at 400 °C in sealed quartz tubes under vacuum. XRD was recorded with a MoK_α source ($\lambda = 0.7107$ Å).

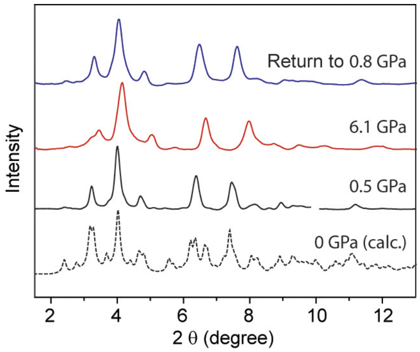

Extended Data Figure 6 | Reversible compression of Cu-S-M9 below 8 GPa. The dashed line shows ambient XRD calculated from the single-crystal structure. The solid lines are *in situ* XRD measured at 0.5 GPa (black), 6.1 GPa (red) and back to 0.8 GPa (blue). $\lambda = 0.6199$ Å.

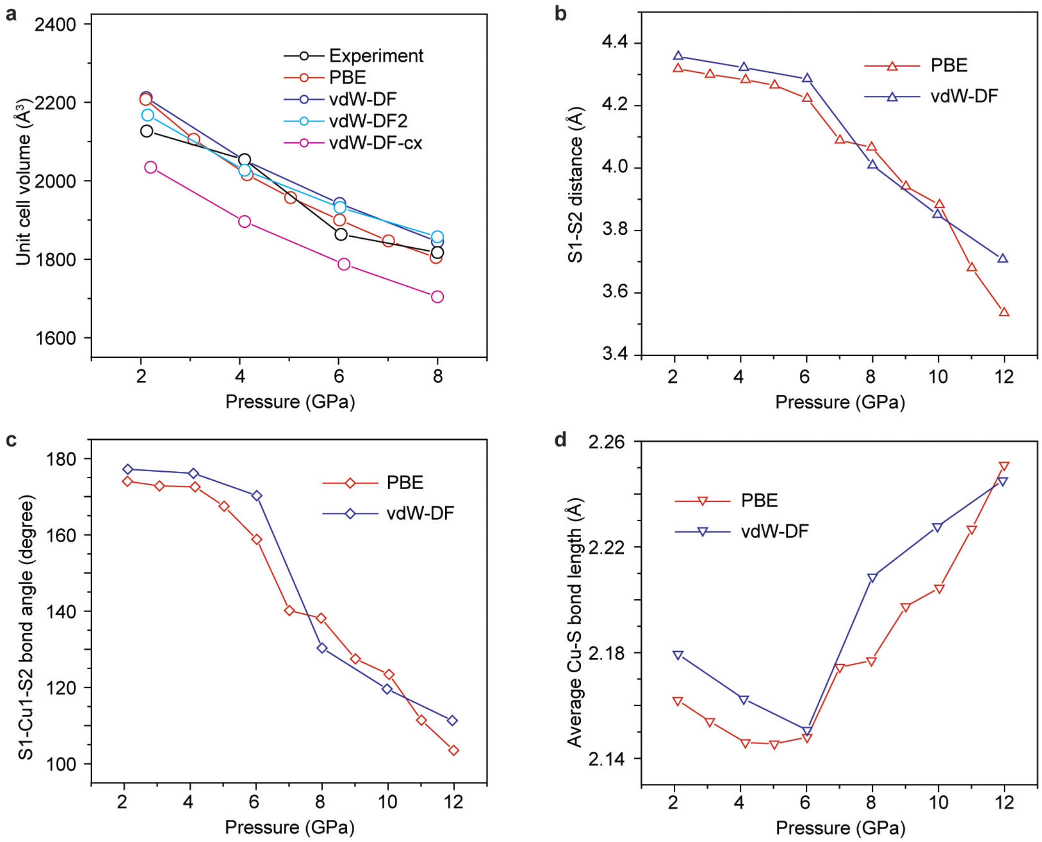

Extended Data Figure 7 | Experimental and computed unit cell volumes and key structural features of Cu-S-M9 at high pressure. a, Unit cell volumes determined by experiment and computed by DFT using different exchange-correlation functionals. **b**–**d**, S1–S2 distance (**b**), S1–Cu1–S2 bond angle (**c**) and average Cu1–S1/Cu1–S2 bond length (**d**) computed using PBE (red) and vdW-DF (blue) functionals. The unit cell volumes computed by PBE, vdW-DF and vdW-DF2 agree well with experimental data, with less than 5% deviation. The vdW-DF-cx functional gave consistently smaller unit cell volume, probably owing to overestimation of the dispersion interaction. Furthermore, PBE and vdW-DF show the same trends in the key structural changes, that is, decreasing S1–S2 distance and S1–Cu1–S2 bond angle, as well as increasing Cu–S bond length beyond 6 GPa. These results show that the van der Waals interactions do not substantially affect the computed high-pressure structures in our systems.

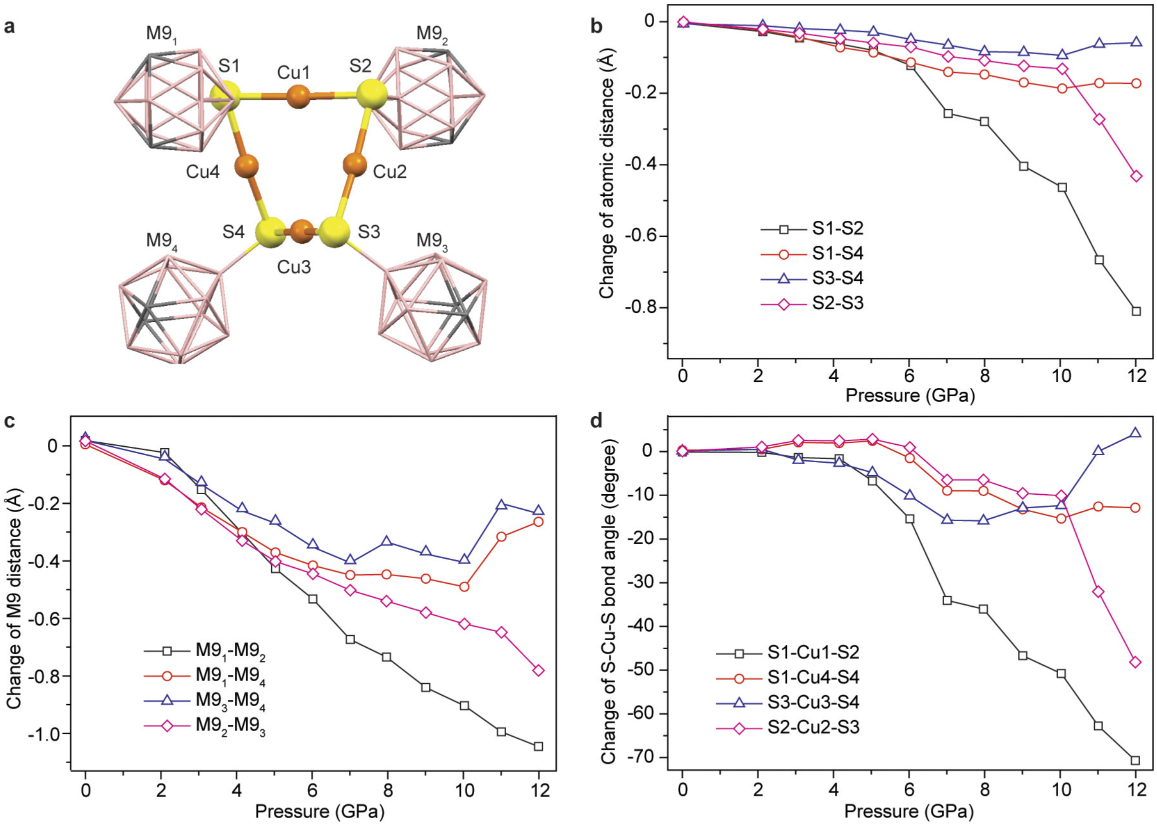

Extended Data Figure 8 | Structural changes of Cu-S-M9 at high pressure. a, Structure of the Cu-S-M9 molecule. **b**–**d**, Changes in S–S distances (**b**), M9–M9 distances (**c**) and S–Cu–S bond angles (**d**) as functions of pressure. All data are extracted from DFT computations.

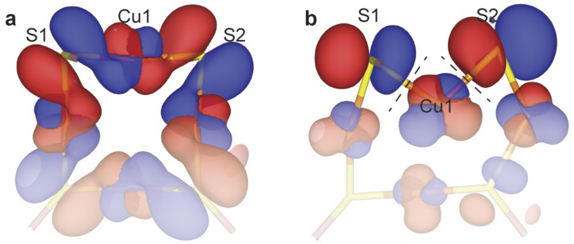

Extended Data Figure 9 | HOMO of Cu-S-M9, uncompressed and compressed. a, At ambient pressure; **b**, at 12 GPa. The isosurfaces depict the probability density times the sign of the HOMO wavefunction ψ. Red and blue represent isovalues of $\pm 2 \times 10^{-4}$ per cubic bohr, respectively. The dashed lines in the 12 GPa structure mark the nodal planes across Cu–S bonds.

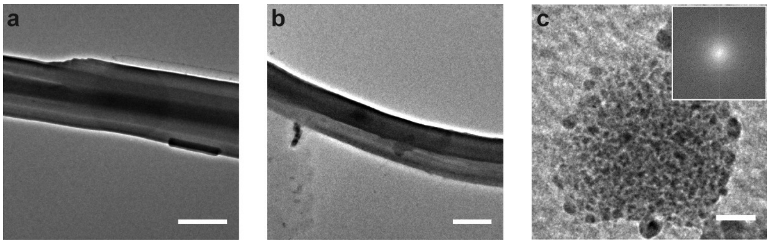

Extended Data Figure 10 | TEM images of sterically impeded systems. **a**, **b**, Cu-S-Ada before (**a**) and after (**b**) 20 GPa compression. Scale bars in **a** and **b**, 1 μm. **c**, Ag-S-Ada after 20 GPa compression. Scale bar, 20 nm. Inset, Fourier transform pattern of **c**.